

accepted for publication in *Cold Regions Science and Technology*

Modelling the interrelationships between permeability, effective porosity and total porosity in sea ice

Chris Petrich

e-mail: cpetrich@physics.otago.ac.nz

Pat J. Langhorne

e-mail: pjl@physics.otago.ac.nz

Zhifa F. Sun

e-mail: zhifa@physics.otago.ac.nz

Affiliation of all authors:

University of Otago, Physics Department, Dunedin, New Zealand

Corresponding author: Chris Petrich,

phone: +64 3 479 7530, fax: +64 3 479 0964

Abstract

A permeability–porosity relationship is obtained for use in computational fluid dynamics (CFD) modelling of desalination and fluid flow in sea ice. This functional relationship is derived from laboratory data from the literature on unidirectional saltwater ice formation. Calibration is performed with the CFD model, combined with field measurements of the stable salinity profile of sea ice. A Monte Carlo percolation model is used to obtain a relationship between effective and total porosity, supporting a simple analytical approximation. Comparison of the permeability–porosity relationship with data from the literature shows consistency within an order of magnitude. Systematic differences could be due to differences in growth conditions.

Keywords: Darcy’s law, Fluid Dynamics, Percolation, Permeability, Porosity, Porous Materials, Sea Ice

1 Introduction

Fluid flow in sea ice is directly relevant to the sea ice heat and mass balances. It is largely responsible for the desalination of growing sea ice that determines the salt flux into the ocean (McPhee and Stanton, 1996; Haarpaintner et al., 2001) and the salinity of young sea ice (Nakawo and Sinha, 1981; Eicken, 1992). In the melt season, it affects the salt budget (Eicken et al., 2002), heat transport (Lytle and Ackley, 1996; Eicken et al., 2002; Kottmeier et al., 2003), and sea ice albedo (Fetterer and Untersteiner, 1998; Haas et al., 2001; Perovich et al., 2002; Eicken et al., 2004). It further affects the sea ice mass balance through surface flooding and snow ice formation (Eicken et al., 1995; Lytle et al., 2000; Maksym and Jeffries, 2000; Kottmeier et al., 2003), and to a lesser extent through meltwater percolation and bottom ice formation (Eicken, 1994; Jeffries et al., 1995; Eicken et al., 2002).

In this paper, a computational fluid dynamics (CFD) model is introduced to simulate fluid flow through sea ice in the absence of air inclusions. The governing equations require a parameterisation of sea ice permeability, Π . Permeability is a function of the structure of the porous ice matrix, and the simplest way to parameterise this structure is through its brine volume fraction, i.e. the total porosity f_t . However, when only fluid flow through the porous medium is of concern, the effective porosity f_e , i.e. the volume fraction of the interconnected pore space, may be a suitable alternative parameter to describe sea ice and its permeability. In either case, the development of preferred flow paths in sea ice affects the permeability–porosity relationship (Freitag, 1999; Freitag and Eicken, 2003). In the present work, we will therefore limit our focus to the development of a permeability–porosity parameterisation appropriate for the case of growing sea ice (Petrich et al., 2004). The total porosity is chosen as a reference since this quantity is directly available in CFD model calculations

as a result of energy and mass conservation. Currently, permeability data for sea ice are scarce, and a relationship between effective and total porosity in sea ice is presently not available. In order to increase the amount of data with which to compare our results, we will therefore make a first attempt to obtain a relationship between total and effective porosity in sea ice.

Consistent with Freitag (1999), the effective porosity refers to the volume fraction of the interconnected pore space (cf. Zhang et al., 1994; Knackstedt and Cox, 1995). However, a definition of effective porosity as the volume fraction of interconnected pore space less the volume fraction of dead-end pores has also been used previously (Koponen et al., 1997).

Permeability parameterisations as functions of total porosity have been used previously in numerical simulations of young sea ice (Medjani, 1996; Maksym and Jeffries, 2000; Oertling and Watts, 2004). Medjani (1996) and Oertling and Watts (2004), in two-dimensional CFD simulations of sea ice growth, treat the frictional effect of sea ice on brine motion by modifying the viscosity of the fluid in regions of large liquid volume fractions, and follow an isotropic permeability parameterisation after Kozeny–Carman for small liquid volume fractions. The parameterisation chosen is not based on measurements. The vertical salinity profiles obtained are of almost homogeneous salinity (Oertling and Watts, 2004), unlike the characteristic C-shape typically observed in sea ice (Weeks and Ackley, 1986). Maksym and Jeffries (2000), in one-dimensional simulations of flooding of sea ice, use a permeability parameterisation after Kozeny–Carman that has been fitted to a few scattered permeability measurements in sea ice (Saeki et al., 1986) and in compacted snow (Kuroiwa, 1968). Compacted snow may, however, be an inadequate model for the columnar sea ice of interest here. In the absence of a suitable permeability parameterisation, we will derive an expression based on an interpretation of laboratory experiments of Cox and Weeks (1975) in NaCl ice. Cox and Weeks investigated the desalination

of artificial sea ice that grows from a constant temperature interface. They obtain data on the rate of desalination as function of total porosity and temperature gradient, which is the foundation for the development in Section 3.

Since there may not be a unique permeability–porosity relationship applicable to sea ice in all situations, we only consider first–year sea ice during the growth season, which is in accord with the experiments of Cox and Weeks (1975). The fluid dynamics simulations treat flow through sea ice as flow through a porous medium (Bear and Bachmat, 1991).

A Monte Carlo percolation model is used to assess the relationship between total and effective porosity. The platelet structure of sea ice is taken into account by discriminating between brine layers, i.e. volumes penetrated by pockets, and ice platelets, i.e. volumes almost inaccessible to pockets. The exclusion of pockets from crystal volumes in percolation models of porous media has previously been applied to different porous materials to explain the magnitude of the critical porosity, f_c , below which the effective porosity vanishes (Janzen, 1975; Kusy, 1977; Golden et al., 1998; Blower, 2001). The present model supposes that the inclusion distribution in sea ice is statistically uniform, which is an assumption that has been used before (Eicken, 1991; Cole et al., 2004).

2 Computational fluid dynamics model

2.1 Introduction

Sea ice growth is treated as the flow of a Newtonian fluid in a two–dimensional domain that is partly pure liquid, and partly porous ice (Bear and Bachmat, 1991). The solid matrix of the porous medium is stationary in position, but time variable as governed by the phase change. The governing equations reduce to the Navier–Stokes equations with the

Boussinesq approximation in the liquid region, while flow in the porous medium is dominated by friction that is expressed through a term after Darcy (Brinkman, 1947). Permeability is treated as a function of local total porosity. The porous medium undergoes phase change, and local thermodynamic equilibrium is assumed. The numerical implementation is based on the finite volume method with a staggered rectangular grid (Patankar, 1980). The set of governing equations are discretised with first-order discretisation schemes, and they are solved iteratively for each time step (Petrich, 2005). The time step is automatically adjusted during the simulation to keep the Courant number, i.e. the ratio between the time step and the characteristic convection time, below 0.1 in all computational cells (Ferziger and Perić, 2002).

2.2 Governing equations

The governing equations are expressed in terms of local, intrinsic volume averages of temperature, T , solute concentration in the liquid, C , and horizontal and vertical fluid velocity components u and v , respectively. The volume averaging method has been used to derive the governing equations (e.g. Ganesan and Poirier, 1990; Bear and Bachmat, 1991; Petrich, 2005). Unless otherwise stated, all physical properties of liquid and solid, for example density and heat capacity, are assumed to be constant locally, i.e. within the averaging volume (representative elementary volume) δV .

The volume-averaged mass conservation equation is

$$\left[1 - \frac{\rho_s}{\rho_l} \right] \frac{\partial f_t}{\partial t} + \frac{\partial(f_t u)}{\partial x} + \frac{\partial(f_t v)}{\partial y} = 0, \quad (1)$$

where u and v are the fluid velocity components in the x and y directions, respectively, f_t is the total porosity, and $\rho_l = 1000 \text{ kg m}^{-3}$ and $\rho_s = 918 \text{ kg m}^{-3}$ are the constant densities of liquid and solid, respectively, that characterise volume change during the phase transition.

The volume-averaged momentum conservation equations are

$$\begin{aligned} \rho_l \left[\frac{\partial(f_t u)}{\partial t} + \frac{\partial(f_t u u)}{\partial x} + \frac{\partial(f_t u v)}{\partial y} \right] \\ = \mu \left[\frac{\partial^2(f_t u)}{\partial x^2} + \frac{\partial^2(f_t u)}{\partial y^2} \right] - f_t \frac{\partial p}{\partial x} - f_t \frac{\mu}{\Pi} f_t u, \quad (2) \end{aligned}$$

$$\begin{aligned} \rho_l \left[\frac{\partial(f_t v)}{\partial t} + \frac{\partial(f_t v u)}{\partial x} + \frac{\partial(f_t v v)}{\partial y} \right] \\ = \mu \left[\frac{\partial^2(f_t v)}{\partial x^2} + \frac{\partial^2(f_t v)}{\partial y^2} \right] - f_t \frac{\partial p}{\partial y} + f_t \rho g - f_t \frac{\mu}{\Pi} f_t v, \quad (3) \end{aligned}$$

where ρ is the variable density of the liquid in the buoyancy term (third term on the right hand side of (3)), which is a function of brine salinity and temperature (Fofonoff and Millard, 1983), $\mu = 1.8 \times 10^{-3} \text{ kg m}^{-1} \text{ s}^{-1}$ is the dynamic viscosity, p the pressure, Π is the characteristic, isotropic permeability of the porous medium, and $g = -9.8 \text{ m s}^{-2}$ is the acceleration due to gravity, which is assumed to be parallel to the y -direction.

The volume-averaged form of the energy balance equation is

$$\begin{aligned} \bar{\rho c} \frac{\partial T}{\partial t} + \rho_l c_l \frac{\partial(f_t u T)}{\partial x} + \rho_l c_l \frac{\partial(f_t v T)}{\partial y} \\ = \frac{\partial}{\partial x} \left[\bar{k} \frac{\partial T}{\partial x} \right] + \frac{\partial}{\partial y} \left[\bar{k} \frac{\partial T}{\partial y} \right] - [T \Delta(\rho c) + L \rho_s] \frac{\partial f_t}{\partial t}, \quad (4) \end{aligned}$$

where T is the temperature of solid and liquid, $L = 334 \times 10^3 \text{ J kg}^{-1}$ is the latent heat of fusion at $T = 0^\circ \text{C}$, and the average quantities in the porous medium are defined as

$$\bar{\rho c} = f_t \rho_l c_l + (1 - f_t) \rho_s c_s, \quad (5)$$

$$\Delta(\rho c) = \rho_l c_l - \rho_s c_s \quad (6)$$

$$\bar{k} = f_t k_l + (1 - f_t) k_s, \quad (7)$$

with the specific heat capacities $c_l = 4.2 \text{ kJ kg}^{-1} \text{ K}^{-1}$ and $c_s = 2.0 \text{ kJ kg}^{-1} \text{ K}^{-1}$, and heat conductivities $k_l = 0.56 \text{ W m}^{-1} \text{ K}^{-1}$ and $k_s = 2.1 \text{ W m}^{-1} \text{ K}^{-1}$ of liquid and solid, respectively.

The volume-averaged solute conservation equation is

$$f_t \frac{\partial C}{\partial t} + \frac{\partial(f_t u C)}{\partial x} + \frac{\partial(f_t v C)}{\partial y} = \frac{\partial}{\partial x} \left[f_t D \frac{\partial C}{\partial x} \right] + \frac{\partial}{\partial y} \left[f_t D \frac{\partial C}{\partial y} \right] - C \frac{\partial f_t}{\partial t}, \quad (8)$$

with the concentration C of solute in the liquid, and the solute diffusion coefficient $D = 3 \times 10^{-10} \text{ m}^2 \text{ s}^{-1}$.

Finally, an equation is needed that governs phase transitions.

Supposing local thermodynamic equilibrium, in any volume δV the temperature T is equal to the freezing point T_F of the brine of concentration C ,

$$T = T_F(C). \quad (9)$$

With consideration given to latent heat release and solute partition at the microscopic interface, (9) constitutes a condition for the change of local liquid volume fraction required to establish thermodynamic equilibrium.

2.3 Freezing front treatment

When simulating sea ice growth, the initial condition is usually a water temperature very close to the freezing point so, if heat is removed, the water quickly becomes supercooled. Since local thermodynamic equilibrium is enforced, supercooling is turned immediately into ice formation. The model in its present form would therefore predict rapid formation of a small ice fraction throughout much of the domain. Depending on the permeability parameterisation imposed this could lead to an artificial flow resistance. In reality, on the scale of the finite volume grid, a freezing front can be defined as having pure liquid on one side, and a porous medium on the other side. To simulate the freezing front, ice formation is allowed only in volumes that either already contain ice, or have a sufficiently high ice fraction, $1 - f_i$, at a minimum of one of their interfaces, where f_i is the liquid volume fraction at the interface. The solid fraction, $1 - f_i$, at the

interface of a cell is calculated from linear extrapolation of the solid fraction of two neighbouring cells (see Figure 1).

A reasonable value for f_i can be estimated from experiments on the solidification of Pb–Sn alloys (Stewart and Weinberg, 1972). Using radioactively tagged lead they find that fluid flowing past the interface penetrates the dendritic interface to the point where the solid volume fraction is $1 - f_t = 0.12$ to 0.22 . Further, the salinity is independent of f_i for $1 - f_i \geq 0.2$, as will be shown in Section 3.3. The solid volume fraction at a cell interface is therefore required to reach $1 - f_i = 0.2$ before ice can form.

3 Permeability from desalination of sea ice

Cox and Weeks (1975) have measured the rate of gravity drainage from laboratory grown sea ice above the skeletal layer. They present data deemed unaffected by brine expulsion, and give a fit function that can be written as

$$\frac{\Delta S_{ice}}{\Delta t} = -A (f_t - f_c) \frac{\Delta T}{\Delta y}, \quad (10)$$

where $A = 3.37 \times 10^{-6} \text{ psu m s}^{-1} \text{ K}^{-1}$ and $f_c = 0.05$ are constants, $f_t > f_c$, and the temperature gradient is $\Delta T / \Delta y > 0$. Since the quality of that fit is not apparent from the figures in linear scale (Cox and Weeks, 1975), the data points of their figures have been resampled (shown in Figure 2), and fitted to a power law (Petrich et al., 2004). The best fit parameters to the equation

$$\frac{\Delta S_{ice}}{\Delta t} = -A (f_t - f_c)^\gamma \frac{\Delta T}{\Delta y}, \quad (11)$$

are $A = 4.2 \times 10^{-6} \text{ psu m s}^{-1} \text{ K}^{-1}$, $f_c = 0.054$, and $\gamma = 1.2$ (Figure 2).

Assuming that, within error, $\Delta S_{ice} = \Delta C_{ice}$, i.e. that a change in salinity (in psu) is equal to a change in concentration (in kg m^{-3}), and that local thermodynamic equilibrium applies, i.e. $\Delta T = m \Delta C$, where m is the slope of the liquidus, equation (11) can be expressed as

$$\frac{\Delta C_{ice}}{\Delta t} = -m A (f_t - f_c)^\gamma \frac{\Delta C}{\Delta y}. \quad (12)$$

By comparing (12) to the one-dimensional solute advection equation in a material of homogeneous porosity (cf. equation (8)),

$$\frac{\partial f_t C}{\partial t} + f_t v \frac{\partial C}{\partial y} = 0, \quad (13)$$

an expression is obtained for the gravity driven, effective desalination mass flow in sea ice during ice growth,

$$f_t v = -m A (f_t - f_c)^\gamma. \quad (14)$$

After substituting (14) into Darcy's law for one-dimensional flow,

$$-\nabla p = \frac{\mu}{\Pi} f_t v, \quad (15)$$

the permeability Π takes on the form

$$\Pi = \frac{\mu m}{\nabla p} A (f_t - f_c)^\gamma. \quad (16)$$

We assume that a single characteristic porosity, f_t , can be used to describe the desalination process in unidirectional sea ice growth in an environment of permeability, Π , and that the driving pressure gradient, ∇p , is approximately independent of the conditions of growth in the cases considered. The characteristic, isotropic permeability, Π , used to describe the desalination process in sea ice is therefore

$$\Pi \propto (f_t - f_c)^\gamma. \quad (17)$$

The constant of proportionality in (17) will be fitted so that the computer model yields realistic salinity profiles. In order to define what is realistic, we exploit the observation of Nakawo and Sinha (1981) that the initial change in the salinity of newly forming sea ice is rapid, but that salinity is relatively constant thereafter. The latter, quasi-constant sea ice salinity, S_{ice} , is termed the stable salinity. Their field data of growth rate, w , and the ratio between stable salinity, S_{ice} , and salinity of the seawater, S_0 , can be fitted to

$$\frac{S_{ice}}{S_0} = 0.19 \left(\frac{w}{w_0} \right)^{0.46}, \quad (18)$$

where the reference velocity, $w_0 = 1.35 \times 10^{-7} \text{ ms}^{-1}$, is the mean freezing front velocity of the data set. Equation (18) is quantitatively similar to the best fit line given by Kovacs (1996) through data of both Nakawo and Sinha (1981) and Wakatsuchi (1983). However, some laboratory experiments (Cox and Weeks, 1975; Eicken et al., 1998) suggest a lower stable salinity, consistent with the sea ice growth model of Cox and Weeks (1988). The model of Cox and Weeks (1988) leads to the relationship

$$\frac{S_{ice}}{S_0} = 0.11 \left(\frac{w}{w_0} \right)^{0.41} \quad (19)$$

for growth velocities between $3 \times 10^{-8} \text{ ms}^{-1} \leq w \leq 3 \times 10^{-6} \text{ ms}^{-1}$ and ice surface temperatures below approximately -14°C (Petrich, 2005).

However, it also suggests that the relationship depends on the air temperature, with ice growing at higher air temperatures exhibiting a lower salinity. Other factors, for example under-ice currents (Feltham et al., 2002), may also influence the salinity of sea ice, and maybe responsible for the difference between (18) and (19).

The computer model from Section 2 is used to find the constant of proportionality in (17) by matching the simulated salinity profiles to the predictions of (18), based on the simulated vertical freezing front velocity.

3.1 Vertical permeability component

Having found a characteristic, isotropic permeability for sea ice, Π , that is suitable for CFD modelling, we now estimate the corresponding vertical permeability component, Π_v , that is suitable for comparison with data in the literature. A transformation between characteristic permeability and the vertical permeability component has previously been applied to experimental data (Freitag, 1999; Freitag and Eicken, 2003; Eicken et al., 2004). However, that transformation is designed for a flow path not applicable to natural desalination of sea ice.

In order to estimate the vertical permeability component from the characteristic permeability, Π , we assume that a typical desalination path exists, and furthermore that the relationship between horizontal $\Pi_{h1,2}$ and vertical Π_v permeability components is well defined (Figure 3). Freitag (1999) reports that even horizontal sea ice permeability is anisotropic, and reports, up to almost one order of magnitude difference between the two orthogonal components Π_{h1} and Π_{h2} . However, for simplicity we follow Freitag and Eicken (2003) by assuming that the relationship between the three orthogonal permeability components in sea ice can be expressed as

$$\Pi_{h1} = \Pi_{h2} = \frac{1}{\kappa} \Pi_v, \quad (20)$$

where κ is the ratio of vertical and horizontal permeability, and the permeability is horizontally isotropic.

Similar to Freitag and Eicken (2003), we further neglect variations of the permeability along the desalination flow path other than due to anisotropy. Defining the flow resistance R as

$$R \propto \frac{1}{\Pi}, \quad (21)$$

the resistance to flow in direction ϕ along an infinitesimal line element ds (Figure 4) is

$$R(\phi) ds = \left[(R_h \cos \phi)^2 + (R_v \sin \phi)^2 \right]^{1/2} ds, \quad (22)$$

where R_h and R_v are proportional to the reciprocals of the horizontal and vertical permeability, respectively. The average flow resistance along flow path l is calculated from

$$R_{avg} = \frac{1}{l} \int_l R(\phi(s)) ds. \quad (23)$$

For the simple case of a path of inflowing seawater and outflowing brine that resembles a half circle (i.e. a simplification of the path sketched

by Worster (1992) and by Wettlaufer et al. (1997)) as illustrated in Figure 4, R_{avg} is expressed as

$$R_{avg} = \frac{1}{\pi} \int_{\pi/2}^{3\pi/2} \left[(R_h \cos \phi)^2 + (R_v \sin \phi)^2 \right]^{1/2} d\phi. \quad (24)$$

With $R_h = \kappa R_v$ from (20) it follows that

$$R_{avg} = R_v \frac{1}{\pi} \int_{\pi/2}^{3\pi/2} \left[1 + (\kappa^2 - 1) \cos^2 \phi \right]^{1/2} d\phi. \quad (25)$$

Equation (25) shows that $R_{avg} = R_v$ for $\kappa = 1$. Further, $R_{avg} = 2/\pi R_v$ as $\kappa \rightarrow 0$, and (25) can be approximated with less than 5% error for $\kappa \geq 3$ by

$$R_{avg} = \frac{2\kappa + 0.5}{\pi} R_v \quad \text{for } \kappa \geq 3, \quad (26)$$

so that from (21),

$$\Pi_v = \frac{2\kappa + 0.5}{\pi} \Pi \quad \text{for } \kappa \geq 3. \quad (27)$$

The half-circle flow path allows us to estimate the vertical permeability component, Π_v , directly from the characteristic permeability, Π , as a function of sea ice anisotropy, κ . The permeability derived from (27) represents the upper limit on vertical permeability (with lower limit $\Pi_v = \Pi$), if the flow path is narrower than assumed. Freitag (1999) finds that the anisotropy of sea ice is $\kappa = 10$ to 100, which according to (27) leads to a vertical permeability that is higher than the isotropic permeability by a factor 7 to 64. Freitag and Eicken (2003) report a typical value of $\kappa = 10$.

3.2 Results for sea ice permeability

The constant of proportionality for the permeability function (17) will be determined next. The requirement imposed on that constant is that it should cause the numerical model developed in Section 2 to produce ice sheets of horizontally averaged vertical salinity profiles predicted by the expression for the stable sea ice salinity (18), based on the simulated vertical sea ice growth velocity, w . The task is reasonably straight-forward with only one parameter to determine.

The ice growth velocity, w , is determined from the time difference between two adjacent rows reaching an average solid fraction above $1 - f_t = 10^{-5}$. The computational domain is periodic in horizontal direction. Initially, the water is of salinity $S_0 = 36$ psu and the temperature is 1 mK above the equilibrium freezing temperature. The upper boundary has a no-slip ($u = v = 0$), constant temperature surface. Since the density of solid and liquid are different, the lower boundary is “open”, allowing fluid to advect into and out of the domain. In the present simulations, $u = 0$ and $\partial v / \partial y = 0$. Fluid advecting into the domain is of the same temperature and salinity as the initial condition of the simulation. Diffusive exchange of solute and heat does not take place across the open boundary.

We find by trial-and-error that

$$\Pi = 1.0 \times 10^{-10} \text{ m}^2 (f_t - 0.054)^{1.2} \quad \text{for } 0.054 < f_t < 1, \quad (28)$$

$\Pi \rightarrow \infty$ for $f_t = 1$, and $\Pi \leq 1 \times 10^{-13} \text{ m}^2$ for $f_t \leq 0.054$ produces appropriate salinity profiles.

Example calculations for ice grown from the upper surface with a constant temperature boundary condition of either -10°C or -20°C in a horizontally periodic domain are shown in Figures 5(a) and (b) (cf. Petrich, 2005). Figure 5(a) is a superposition of three scatter plots at -10°C and five scatter plots at -20°C for calculations with various grid and domain sizes. A certain amount of scatter that resembles natural variability of salinity profiles (Bennington, 1967; Cottier et al., 1999) is clearly visible. The bottom sections of the profiles where the salinity profile has not yet been stabilised are not shown for clarity. Figure 5(b) shows two example profiles with particularly little scatter. The domain size is $1.28 \text{ m} \times 1.28 \text{ m}$, and the grid is 16×16 . The salinity profiles follow the typical C-shape.

Using (27), the expected vertical permeability is, with an anisotropy of $\kappa = 10$,

$$\Pi_v = 7 \times 10^{-10} \text{ m}^2 (f_t - 0.054)^{1.2}. \quad (29)$$

3.3 Influence of freezing front definition on the salinity profile

Since the seawater is at its freezing temperature, a freezing interface definition has been introduced in Section 2.3. According to this definition, ice formation can be initiated in a cell only if the porosity at any of its boundaries falls below the free parameter f_i . The sensitivity of the salinity profiles to f_i will be investigated in this section.

One consequence of the introduction of a constraint on freezing is that water is allowed to supercool in purely liquid cells. This leads to an ocean heat flux if the water is advected through the open boundary since water advected into the domain is hotter. For a sea ice sheet of thickness 1.08 m, Table 1 lists the mean conductive heat flow through the upper boundary, \overline{F}_c , the mean advective heat flow through the bottom boundary, \overline{F}_a , and the sum of the mean rate of latent and sensible heat stored within the domain, \overline{F}_h . The mean heat flows are defined as

$$\overline{F}_c = \frac{1}{t_{1.08\text{m}}} \frac{1}{x_0} \int_0^{t_{1.08\text{m}}} \int_0^{x_0} \left(k \frac{\partial T}{\partial y} \right) dx dt \quad \text{at } y = y_{\text{top}}, \quad (30)$$

$$\overline{F}_a = \frac{1}{t_{1.08\text{m}}} \frac{1}{x_0} \int_0^{t_{1.08\text{m}}} \int_0^{x_0} \rho_l c_l (vT) dx dt \quad \text{at } y = y_{\text{bottom}}, \quad (31)$$

with positive flows being into the domain, and

$$\overline{F}_h = \frac{1}{t_{1.08\text{m}}} \frac{1}{x_0 y_0} \int_0^{y_0} \int_0^{x_0} \left\{ [T\Delta(\rho c) - (1 - f_t)L\rho_s]_{t=t_{1.08\text{m}}} - [T\Delta(\rho c) - (1 - f_t)L\rho_s]_{t=0} \right\} dx dy, \quad (32)$$

where $x_0 = 0.72$ m and $y_0 = 1.44$ m are the horizontal and vertical extent of the domain, respectively, and $t_{1.08\text{m}}$ is the time at that the freezing interface has reached 1.08 m. The heat flows balance, i.e. $\overline{F}_c + \overline{F}_a = \overline{F}_h$, illustrating that the simulations are consistent. The ocean heat flow, \overline{F}_a , increases with increasing solid volume fraction at the interface, $1 - f_i$, leading to an increased time for ice formation, $t_{1.08\text{m}}$. In reality, most of the supercooling would probably be released by growing ice platelets.

Profiles of horizontally averaged sea ice salinity are shown in Figure 6, and compared with the profiles expected from the actual growth velocity, w , based on equation (18). The expected salinity profiles for $0.1 \leq 1 - f_i \leq 0.5$ coincide with each other to within 1 psu, the differences being due to the f_i -dependence of the growth velocity (see above). The expected profile for $1 - f_i = 0.8$ is significantly smaller for the same reason. Predictions close to the upper interface of the ice sheet are unreliable since they are based on growth velocities outside the scope of equation (18). The high salinity data in the upper 120 mm show that desalination of sea ice begins after a critical thickness is reached. A similar effect has been described before for laboratory experiments (Wettlaufer et al., 1997). The sea ice salinity is systematically higher than predicted from (18) at the bottom 120 mm since the ice is still in the process of desalination.

In spite of vastly different growth rates, the average salinity profiles do not show an obvious dependence on f_i for $1 - f_i \geq 0.2$. Since the temperature gradient at the time of ice formation at a given depth is independent of f_i , this may indicate that sea ice desalination is more strongly affected by the vertical temperature gradient than by the velocity of the freezing front. Temperature gradient and growth velocity would be proportional to each other only in the absence of an ocean heat flux. Occasional incomplete desalination in regions of originally downflowing brine leads to scatter in the salinity plots.

4 Percolation approach to the relationship between total and effective porosity

4.1 Model description

In order to enable the comparison of (29) with data of Freitag (1999), a relationship between total porosity, f_t , and effective porosity, f_e , is sought

using a simple Monte Carlo model (Petrich and Langhorne, 2005). Pockets, representing brine inclusions, are added into a domain, representing sea ice, and the relationship between total porosity and effective porosity is evaluated.

In this model, the sea ice sheet is a cubical domain that is riddled with pockets shaped as rectangular boxes. Rectangular boxes are chosen as the exact calculation of both total and effective porosities is possible and even trivial. Pockets are aligned with the sides of the domain. The model is continuous, i.e. no grid is used. In the course of the simulation, pockets are sequentially inserted into the domain at random locations. The pockets have a “soft core”, i.e. they may overlap. If pockets overlap they form a cluster. After a pocket has been added the total porosity, f_t , of the domain is calculated, accounting for pocket overlap, and the total volume that is occupied by clusters that connect to both the top boundary and the bottom boundary is determined (y -direction). The latter volume is the effective porosity, f_e . The domain is periodic in x and in z -directions in order to reduce finite size effects. The random number generator used is *Mersenne Twister* (Matsumoto and Nishimura, 1998; Nishimura, 2000), implemented as `mt19937ar.c`, 26 January, 2002, by Makoto Matsumoto and Takuji Nishimura with 53 bit number generation due to Isaku Wada.

The Monte Carlo model is validated by determining the critical porosity in both two and three dimensions. As shown by Petrich (2005), the critical porosities for squares in two dimensions and for cubes in three dimensions are determined to be $f_c^{2D} = 0.667 \pm 0.001$ and $f_c^{3D} = 0.277 \pm 0.001$, respectively. These results are in agreement with the results of Baker et al. (2002), $f_c^{2D} = 0.6666 \pm 0.0004$ and $f_c^{3D} = 0.2773 \pm 0.0002$.

The platelet structure of sea ice is approximated by a sandwich layer model of alternating brine layers and ice platelets as illustrated in Figure 7

and described by Perovich and Gow (1996). An attempt is made to add pockets to the domain at random locations. If they fall completely into a brine layer, treatment is as described above. If they partially or completely fall into the domain of a platelet, however, they are added only if they connect to an existing cluster.

The physical significance of this difference is that clusters are allowed to come into existence and to grow in brine layers, while, in platelets, clusters are only allowed to grow. The cluster creation is similar to an observation of Perovich and Gow (1996). At first glance they find, upon warming, that brine inclusions seem to appear at random locations. Closer investigation, however, revealed that inclusions already existed at those locations, but that their sizes were below the detection limit. A similar observation has been made by Eicken et al. (2000). The insertion of pockets into the brine layers is therefore equivalent to preexisting brine inclusions reaching the detection limit. On the other hand, the prohibition of pocket insertion in the platelet regions means that the only way for inclusions to interfere with the platelets is by melting or dissolving into them.

We anticipate that this model will produce a percolation threshold, f_c , that can be calibrated by adjusting brine layer thickness, d_0 , and platelet spacing, a_0 , of the stacking sequence in Figure 7. Further, we expect that the model will yield the desired relationship $f_e = f_t$ for $f_t \rightarrow 1$, i.e. in the skeletal layer.

4.2 Results for effective porosity vs. total porosity

4.2.1 Numerical determination

Figures 8(a) and (b) show the relationship between effective and total porosity for three example calculations: a two-dimensional domain of 2000×2000 , a three-dimensional domain of $200 \times 200 \times 200$, and a sandwich domain of $a_0 = \Delta x = 1000$, $d_0 = 195.1$, and $\Delta y = \Delta z = 200$,

respectively. The relationship between a_0 and d_0 has been selected to yield a critical porosity of $f_c = 0.054$, which is the critical porosity that is used in the permeability function (28).

It is clear from Figure 8(a) that a relationship $f_e = f_t$ is approached for $f_t \rightarrow 1$, as expected. Figure 8(b) shows the relationship between f_e and $f_t - f_c$. From percolation theory it is expected for an infinite system that

$$f_e = \alpha (f_t - f_c)^\beta \quad \text{for } f_t \gtrsim f_c, \quad (33)$$

where $\beta \approx 0.14$ in two dimensions, and $\beta \approx 0.41$ in three dimensions (Stauffer and Aharony, 1992; Sahimi, 1993), and α is an undetermined constant of proportionality. In infinite systems, the effective porosity is the volume fraction of the infinite cluster. The straight portions of the double logarithmic plot of Figure 8(b) can be approximated by the power law (33) with best-fit parameters summarised in Table 2. The parameters α and β are determined from averages of three runs each of which produced a critical porosity to within ± 0.001 of the expected value for the cases of two and three dimensions. The parameters α , β , and f_c for the sandwich model are averages of 16 runs. The exponents β are close to the expected values for two and three-dimensional systems, respectively.

With parameters from Table 2 for the sandwich model, the relationship between effective and total porosities is

$$f_e = \begin{cases} 0 & \text{for } f_t \leq 0.054, \\ 0.34 (f_t - 0.054)^{0.41} & \text{for } 0.054 < f_t \leq 0.09, \\ f_t & \text{for } 0.09 < f_t, \end{cases} \quad (34)$$

where $f_x = f_t = 0.09$ is the porosity at which the discontinuity in f_e is minimised. (Equation (34) has a discontinuity in f_e of 0.003 at $f_t = 0.09$.)

4.2.2 Analytical approximation

Since the discontinuity at f_x is small compared to the scatter expected in experiments (e.g. Zhang et al., 1994), we may approximate the relationship

between effective and total porosity based on the expectation from percolation theory (33), and the equality of effective and total porosity for $f_t \rightarrow 1$. Therefore, using the approximate form

$$f_e \approx \begin{cases} 0 & \text{for } f_t \leq f_c, \\ \alpha(f_t - f_c)^\beta & \text{for } f_c < f_t \leq f_x, \\ f_t & \text{for } f_x < f_t, \end{cases} \quad (35)$$

we suppose that (35) and its first derivative are continuous at a transfer porosity f_x . In this case, f_x and α can be expressed as functions of f_c , i.e.

$$f_x = \frac{f_c}{1 - \beta}, \quad (36)$$

and

$$\alpha = \frac{1}{\beta} \left(f_c \frac{\beta}{1 - \beta} \right)^{1-\beta}. \quad (37)$$

For a random percolating system in three dimensions ($\beta = 0.41$) with $f_c = 0.054$ we can calculate from (36) and (37) that $\alpha = 0.352$ and $f_x = 0.0915$, similar to (34). Using the same arguments in porous systems without excluded volume we have in the two ($\beta = 0.139$, squares $f_c = 0.667$) and three ($\beta = 0.41$, cubes $f_c = 0.277$) dimensional cases, $\alpha = 1.056$ and $\alpha = 0.923$, respectively, which compares well with the results in Table 2.

Although suitable data for sea ice are presently not available, experimental data relating effective porosity to total porosity have been obtained for compressed calcite aggregates (Zhang et al., 1994). Comparing measurements of total and effective porosity, Zhang et al. find that $f_e = f_t$ for high porosities, but deviates from equality for $f_t < f_x = 0.07$. They further note that the effective porosity vanishes for total porosities below $f_t \leq f_c = 0.04$. While they do not discuss the relationship between f_c and f_x , we note that their observation is consistent with (36) with $\beta = 0.41$.

4.2.3 Applicability of parameters a_0 and d_0

A ratio between brine layer width and platelet spacing of $d_0/a_0 = 195.1/1000$ has been selected as it results in the desired critical

porosity of $f_c = 0.054$ for the sandwich model. This ratio is realistic for sea ice, as shall be shown now.

Anderson and Weeks (1958) find that the brine film between platelets breaks up into individual, discernable brine inclusions when its width falls below $70 \mu\text{m}$. Using the development of Nakaya (1956), they reason from the resulting mean inclusion size and separation that the break-up into inclusions may be governed by surface tension. However, they did not propose a reason for a value of $70 \mu\text{m}$.

Assuming that microscopic inclusions form within the volume of the original brine film width, $70 \mu\text{m}$ is the brine layer width, d_0 , of the sandwich model above. The brine layer width, d_0 , is thus invariant during subsequent temperature decrease, even though the size of the brine inclusions is temperature dependent. For a brine layer width of $d_0 = 70 \mu\text{m}$, the corresponding platelet spacing is $a_0 = 70 \mu\text{m} \times 1000/195 = 360 \mu\text{m}$. The platelet spacing of sea ice varies weakly with the ice growth velocity (Weeks and Ackley, 1986). The expressions given by Lofgren and Weeks (1969) and Nakawo and Sinha (1984) both show that a platelet spacing of $a_0 = 360 \mu\text{m}$ can be expected at a growth velocity of $2.8 \times 10^{-7} \text{ms}^{-1}$, which is a realistic value for sea ice.

5 Results and analysis

5.1 Comparison of permeability–porosity relationships

We will compare the vertical permeability parameterisation obtained in this paper with bail test measurements in the Arctic and with laboratory experiments.

From bail test measurements in the Arctic, Freitag (1999) gives two relationships between the vertical permeability and effective porosity. They

are, in our notation, for young first-year sea ice

$$\Pi_v = 3 \times 10^{-8} \text{ m}^2 f_e^{3.9} \quad \text{for } 0.05 \leq f_e \leq 0.2, \quad (38)$$

and for old first-year, multiyear, and ridged sea ice

$$\Pi_v = 6 \times 10^{-10} \text{ m}^2 f_e^{1.6} \quad \text{for } 6 \times 10^{-4} \leq f_e \leq 0.6. \quad (39)$$

Data scatter by ± 0.5 orders of magnitude in the case of young first-year sea ice, and by ± 1 order of magnitude in the case of old sea ice.

Eicken et al. (2004) give the following best fit line from bail test measurements for the vertical permeability as a function of total porosity,

$$\Pi_v = \begin{cases} 4.708 \times 10^{-14} \text{ m}^2 \exp(76.90 f_t) & \text{for } f_t \leq 0.096, \\ 3.738 \times 10^{-11} \text{ m}^2 \exp(7.265 f_t) & \text{for } f_t > 0.096. \end{cases} \quad (40)$$

However, details of the investigated sea ice are not given, data are not shown, and the outer limits of the porosity range are not stated. Figure 9 shows the vertical permeability–total porosity relationship (29) (this work), (38) (Freitag, young ice, scaled with (34)), (39) (Freitag, old ice, scaled with (34)), and (40) (Eicken et al. (2004)). Also plotted for reference are the data of Cox and Weeks (1975) on which the permeability function of this work is based, scaled according to the development in Section 3.

Maksym and Jeffries (2000) compile laboratory measurements of sea ice permeability of three groups. They estimate the porosity of the investigated sea ice in two instances (Saito and Ono, 1978; Ono and Kasai, 1985), where porosity measurements were not given. Sea ice permeability data given by Maksym and Jeffries (2000) in their figure 3 are also shown in Figure 9.

Although derived from different sea ice samples, the permeability measurements shown in Figure 9 agree in order of magnitude with the permeability–porosity relationship of this paper.

6 Discussion and conclusion

A two-dimensional computational fluid dynamics model has been introduced to simulate fluid flow through sea ice, including the effects of phase transition and volume expansion during freezing. Although applied to unidirectional sea ice formation in this paper, it may be useful for modelling fluid flow in more complex geometries, such as refreezing cracks (Petrich et al., 2003; Petrich, 2005).

Based on laboratory experiments of Cox and Weeks (1975), calibrated with field experiments of Nakawo and Sinha (1981), a permeability–porosity parameterisation has been developed that is suitable for the simulation of desalination during unidirectional sea ice growth. This permeability–porosity relationship is in quantitative agreement with measurements of other groups. However, there is considerable scatter among these measurements that may arise because the stable salinity of sea ice is not a function of growth velocity, only. As a result, sea ice permeability may be somewhat dependent on growth conditions, contributing to these differences between experiments.

Complete desalination of the sea ice sheet is prevented in the present computational fluid dynamics simulation by a strong reduction of permeability as the total porosity reaches a critical value, f_c . However, the development of pore space that is disconnected from the flow path should in fact contribute to solute retention significantly (Petrich, 2005). Since the pore space model is not included in the CFD model used to derive the permeability expression, the permeability parameterisations (28) and (29) could possibly underestimate sea ice permeability at total porosities of the order of f_c .

A relationship between effective and total porosity has been developed for the case of randomly overlapping pockets of equal size in infinite domains with excluded volume. It has been shown that the numerically

obtained relationship can be approximated by simple analytical considerations. The result has been successfully compared to experimental data on compressed calcite aggregates, however, there is presently insufficient data available for a comparison in sea ice.

The developed relationship between effective and total porosity applies to samples of homogeneous structure, which enters the approximations through the critical porosity f_c . Errors can be expected if the investigated sample spans layers that differ structurally. However, if the sample size is too small, the measured effective porosity will be larger than the effective porosity modelled for an infinite system at porosities close to the critical porosity due to the fractal character of the infinite cluster (Stauffer and Aharony, 1992).

An interesting implication of the porosity model is that the critical porosity of sea ice, f_c , depends on the structure of the ice, expressed through brine layer width, d_0 , brine layer spacing, a_0 , and f_c^{3D} through (Janzen, 1975)

$$f_c = \frac{d_0}{a_0} f_c^{3D}. \quad (41)$$

The value of the critical porosity f_c^{3D} depends on the pocket shape (de Bondt et al., 1992; Xia and Thorpe, 1988; Garboczi et al., 1995; Baker et al., 2002; Yi and Sastry, 2004) and on the pocket distribution (Rintoul, 2000; Blower, 2001; Consiglio et al., 2003; Gaonac'h et al., 2003). As discussed above, the ratio d_0/a_0 depends on the conditions at the time of sea ice formation. Currently, there are no experimental data available for sea ice that test the relationship between structure and critical porosity.

Some of the ideas applied in this work call for further experimental investigation. In particular, there is an experimental deficit of work on the stable salinity of sea ice, and on the relationship between effective and total porosity in sea ice.

Acknowledgements

This work was supported by the Foundation for Research, Science and Technology, New Zealand. CP wishes to acknowledge financial support of the University of Otago Postgraduate Scholarship, of the University of Otago Bridging Grant, and of the Beverly Fund of the University of Otago. Early comments of Joe Trodahl on the percolation simulations are acknowledged. Hajo Eicken is thanked for kindly providing INTERICE data, and Greg Leonard and Craig Purdie for their support of the numerical simulations.

References

- Anderson, D. L., and W. F. Weeks (1958). A theoretical analysis of sea ice strength. *American Geophysical Union, Transactions*, 39(4), 632–640.
- Baker, D. R., G. Paul, S. Sreenivasan, and H. E. Stanley (2002). Continuum percolation threshold for interpenetrating squares and cubes. *Physical Review E*, 66, 046136.
- Bear, J., and Y. Bachmat (1991). *Introduction to Modeling of Transport Phenomena in Porous Media. Theory and Application of Transport in Porous Media*, vol. 4. Kluwer Academic Publishers, Dordrecht, The Netherlands.
- Bennington, K. O. (1967). Desalination features in natural sea ice. *Journal of Glaciology*, 6(48), 845–857.
- Blower, J. D. (2001). Factors controlling permeability–porosity relationships in magma. *Bulletin of Volcanology*, 63, 497–504.
- de Bondt, S., L. Froyen, and A. Deruyttere (1992). Electrical conductivity of composites: A percolation approach. *Journal of Materials Science*, 27, 1983–1988.
- Brinkman, H. C. (1947). A calculation of the viscous force exerted by a flowing fluid on a dense swarm of particles. *Applied Science Research A*, 1, 27–34.
- Cole, D. M., H. Eicken, K. Frey, and L. H. Shapiro (2004). Observations of banding in first–year Arctic sea ice. *Journal of Geophysical Research*, 109, C08012. doi:10.1029/2003JC001993.

- Consiglio, R., D. R. Baker, G. Paul, and H. E. Stanley (2003). Continuum percolation thresholds for mixtures of spheres of different sizes. *Physica A*, 319, 49–55.
- Cottier, F., H. Eicken, and P. Wadhams (1999). Linkages between salinity and brine channel distribution in young sea ice. *Journal of Geophysical Research*, 104(C7), 15,859–15,871.
- Cox, G. F. N., and W. F. Weeks (1975). Brine drainage and initial salt entrapment in sodium chloride ice. Research Report 345. Cold Regions Research and Engineering Laboratory. Hanover, NH, USA.
- Cox, G. F. N., and W. F. Weeks (1988). Numerical simulations of the profile properties of undeformed first-year sea ice during the growth season. *Journal of Geophysical Research*, 93(C10), 12,449–12,460.
- Eicken, H. (1991). Quantification of sea-ice properties: Automated image analysis of thin sections and parameterization of chlorophyll and salinity distributions. *Berichte zur Polarforschung*, 82. In German.
- Eicken, H. (1992). Salinity profiles of Antarctic sea ice: Field data and model results. *Journal of Geophysical Research*, 97(C10), 15,545–15,557.
- Eicken, H. (1994). Structure of under-ice melt ponds in the central Arctic and their effect on the sea ice cover. *Limnology and Oceanography*, 39, 682–694.
- Eicken, H., H. Fischer, and P. Lemke (1995). Effects of the snow cover on Antarctic sea ice and potential modulation of its response to climate change. *Annals of Glaciology*, 21, 369–376.
- Eicken, H., J. Weissenberger, I. Bussmann, J. Freitag, W. Schuster, F. Valero Delgado, K.-U. Evers, P. Jochmann, C. Krembs, R. Gradinger, F. Lindemann, F. Cottier, R. Hall, P. Wadhams, M. Reiemann, H. Kousa, J. Ikävalko, G. H. Leonard, H. Shen, S. F. Ackley, and L. H. Smedsrud (1998). Ice-tank studies of physical and biological sea-ice processes. *Ice in Surface Waters. Proceedings of the 14th International Symposium on Ice*, edited by H. T. Shen. pp. 363–370.
- Eicken, H., C. Bock, R. Wittig, H. Miller, and H.-O. Poertner (2000). Magnetic resonance imaging of sea-ice pore fluids: Methods and thermal evolution of pore microstructure. *Cold Regions Science and Technology*, 31, 207–225.
- Eicken, H., H. R. Krouse, D. Kadko, and D. K. Perovich (2002). Tracer studies of pathways and rates of meltwater transport through Arctic summer sea ice. *Journal of Geophysical Research*, 107(C10), 8046. doi:10.1029/2000JC000583.

- Eicken, H., T. C. Grenfell, D. K. Perovich, J. A. Richter-Menge, and K. Frey (2004). Hydraulic controls of summer Arctic pack ice albedo. *Journal of Geophysical Research*, 109, C08007. doi:10.1029/2003JC001989.
- Feltham, D. L., M. G. Worster, and J. S. Wettlaufer (2002). The influence of ocean flow on newly forming sea ice. *Journal of Geophysical Research*, 107(C2), 3009.
- Ferziger, J. H., and M. Perić (2002). *Computational Methods for Fluid Dynamics*. 3rd ed.. Springer-Verlag, Berlin, Germany.
- Fetterer, F., and N. Untersteiner (1998). Observations of melt ponds on Arctic sea ice. *Journal of Geophysical Research*, 103(C11), 24,821–24,835.
- Fofonoff, N. P., and R. C. Millard (1983). Algorithms for computation of fundamental properties of seawater. *Unesco Technical Papers in Marine Science* 44. Unesco. Paris, France.
- Freitag, J. (1999). The hydraulic properties of Arctic sea ice – implications for the small scale particle transport. *Berichte zur Polarforschung*, 325. In German.
- Freitag, J., and H. Eicken (2003). Meltwater circulation and permeability of Arctic summer sea ice derived from hydrological field experiments. *Journal of Glaciology*, 49(166), 349–358.
- Ganesan, S., and D. R. Poirier (1990). Conservation of mass and momentum for the flow of interdendritic liquid during solidification. *Metallurgical Transactions B*, 21B(1), 173–181.
- Gaonac’h, H., S. Lovejoy, and D. Schertzer (2003). Percolating magmas and explosive volcanism. *Geophysical Research Letters*, 30(11), 1559. doi:10.1029/2002GL016022.
- Garboczi, E. J., K. A. Snyder, J. F. Douglas, and M. F. Thorpe (1995). Geometrical percolation–threshold of overlapping ellipsoids. *Physical Review E*, 52(1), 819–828. Part B.
- Golden, K. M., S. F. Ackley, and V. I. Lytle (1998). The percolation phase transition in sea ice. *Science*, 282(5397), 2238–2241.
- Haarpaintner, J., J.-C. Gascard, and P. M. Haugan (2001). Ice production and brine formation in Storfjorden, Svalbard. *Journal of Geophysical Research*, 106(C7), 14,001–14,013.
- Haas, C., D. N. Thomas, and J. Bareiss (2001). Surface properties and processes of perennial Antarctic sea ice in summer. *Journal of Glaciology*, 47(159), 613–625.
- Janzen, J. (1975). On the critical conductive filler loading in antistatic composites. *Journal of Applied Physics*, 46(2), 966–969.

- Jeffries, M. O., K. Schwartz, K. Morris, A. D. Veazey, H. R. Krouse, and S. Cushing (1995). Evidence for platelet ice accretion in Arctic sea ice development. *Journal of Geophysical Research*, 100(C6), 10,905–10,914.
- Knackstedt, M. A., and S. F. Cox (1995). Percolation and the pore geometry of crustal rocks. *Physical Review E*, 51(6), R5181–R5184.
- Koponen, A., M. Kataja, and J. Timonen (1997). Permeability and effective porosity of porous media. *Physical Review E*, 56(3), 3319–3325.
- Kottmeier, C., K. Frey, M. Hasel, and O. Eisen (2003). Sea ice growth in the eastern Weddell Sea in winter. *Journal of Geophysical Research*, 108(C4), 3125. doi:10.1029/2001JC001087.
- Kovacs, A. (1996). Sea ice: Part I. Bulk salinity versus ice floe thickness. Report 96–7. Cold Regions Research and Engineering Laboratory. Hanover, NH, USA.
- Kuroiwa, D. (1968). Liquid permeability of snow. IUGG/IASH General Assembly of Bern, 25 Sept.–7 Oct. 1967, Commission of Snow and Ice, edited by W. Ward. Publication 79. pp. 380–391. International Association of Scientific Hydrology, Gentbrugge, Belgium.
- Kusy, R. P. (1977). Influence of particle–size ratio on continuity of aggregates. *Journal of Applied Physics*, 48(12), 5301–5305.
- Lofgren, G., and W. F. Weeks (1969). Effect of growth parameters on substructure spacing in NaCl ice crystals. *Journal of Glaciology*, 8(52), 153–164.
- Lytle, V. I., and S. F. Ackley (1996). Heat flux through sea ice in the Western Weddell Sea: Convective and conductive transfer processes. *Journal of Geophysical Research*, 101(C4), 8853–8868.
- Lytle, V. I., R. Massom, N. Bindoff, A. Worby, and I. Allison (2000). Wintertime heat flux to the underside of East Antarctic pack ice. *Journal of Geophysical Research*, 105(C12), 28,759–28,769.
- Maksym, T., and M. O. Jeffries (2000). A one–dimensional percolation model of flooding and snow ice formation on Antarctic sea ice. *Journal of Geophysical Research*, 105(C11), 26,313–26,331.
- Matsumoto, M., and T. Nishimura (1998). Mersenne Twister: A 623–dimensionally equidistributed uniform pseudorandom number generator. *ACM Transactions on Modeling and Computer Simulation*, 8(1), 3–30.
- McPhee, M. G., and T. P. Stanton (1996). Turbulence in the statically unstable oceanic boundary layer under Arctic leads. *Journal of Geophysical Research*, 101(C3), 6409–6428.

- Medjani, K. (1996). Numerical simulation of the formation of brine pockets during the freezing of the NaCl–H₂O compound from above. *International Communications in Heat and Mass Transfer*, 23(7), 917–928.
- Nakawo, M., and N. K. Sinha (1981). Growth rate and salinity profile of first-year sea ice in the high Arctic. *Journal of Glaciology*, 27(96), 315–330.
- Nakawo, M., and N. K. Sinha (1984). A note on brine layer spacing of first-year sea ice. *Atmosphere–Ocean*, 22(2), 193–206.
- Nakaya, U. (1956). Properties of single crystals of ice, revealed by internal melting. Research Paper 13. Cold Regions Research and Engineering Laboratory. Hanover, NH, USA.
- Nishimura, T. (2000). Tables of 64-bit Mersenne Twisters. *ACM Transactions on Modeling and Computer Simulation*, 10(4), 348–357.
- Oertling, A. B., and R. G. Watts (2004). Growth of and brine drainage from NaCl–H₂O freezing: A simulation of young sea ice. *Journal of Geophysical Research*, 109, C04013. doi:10.1029/2001JC001109.
- Ono, N., and T. Kasai (1985). Surface layer salinity of young sea ice. *Annals of Glaciology*, 6, 298–299.
- Patankar, S. V. (1980). *Numerical Heat Transfer and Fluid Flow*. Hemisphere Publishing Co., New York, NY, USA.
- Perovich, D. K., and A. J. Gow (1996). A quantitative description of sea ice inclusions. *Journal of Geophysical Research*, 101(C8), 18,327–18,343.
- Perovich, D. K., T. C. Grenfell, B. Light, and P. V. Hobbs (2002). Seasonal evolution of the albedo of multiyear Arctic sea ice. *Journal of Geophysical Research*, 107(C10), 8044. doi:10.1029/2001JC000438.
- Petrich, C. (2005). Growth, structure, and desalination of refreezing cracks in sea ice. Ph.D. thesis. University of Otago. Dunedin, New Zealand.
- Petrich, C., and P. J. Langhorne (2005). On the relationship between effective and total pore space in sea ice. *Proceedings of the 18th International Conference Port and Ocean Engineering under Arctic Conditions*, Potsdam, New York, USA, June 26-30, 2005, vol. 2, edited by J. P. Dempsey. pp. 883–892.
- Petrich, C., T. G. Haskell, and P. J. Langhorne (2003). Structure of refrozen cracks in first-year sea ice. *Canadian Journal of Physics*, 81(1–2), 293–299.
- Petrich, C., P. J. Langhorne, and Z. Sun (2004). Numerical simulation of sea ice growth and desalination. *Proceedings of the 17th IAHR International Symposium on Ice*, vol. 3. All-Russian Research Institute of Hydraulic Engineering (VNIIG), St. Petersburg, Russian Federation. In press.

- Rintoul, M. D. (2000). Precise determination of the void percolation threshold for two distributions of overlapping spheres. *Physical Review E*, 62(1), 68–72.
- Saeki, H., T. Takeuchi, M. Sakai, and E. Suenaga (1986). Experimental study on permeability coefficients of sea ice. *Ice Technology, Proceedings of the 1st International Conference, Cambridge, Mass. USA*, edited by T. K. S. Murthy, J. J. Connor, and C. A. Brebbia. pp. 237–246. Springer–Verlag, Berlin, Germany.
- Sahimi, M. (1993). Nonlinear transport process in disordered media. *AIChE Journal*, 39(3), 369–386.
- Saito, T., and N. Ono (1978). Percolation in sea ice, I, Measurements of kerosene permeability of NaCl ice. *Teion-Kagaku (Low Temperature Science), Series A*, 37, 55–62.
- Stauffer, D., and A. Aharony (1992). *Introduction to Percolation Theory*. 2nd ed.. Taylor and Francis, London, UK.
- Stewart, M. J., and F. Weinberg (1972). Fluid flow through a solid–liquid dendritic interface. *Metallurgical Transactions*, 3(1), 333–337.
- Wakatsuchi, M. (1983). Brine exclusion process from growing sea ice. *Teion-Kagaku (Low Temperature Science)*, A33, 29–65.
- Weeks, W. F., and S. F. Ackley (1986). The growth, structure, and properties of sea ice. *The Geophysics of Sea Ice, NATO ASI Series, Series B: Physics*, vol. 146, edited by N. Untersteiner. pp. 9–164. Plenum Press, New York, NY, USA.
- Wettlaufer, J. S., M. G. Worster, and H. E. Huppert (1997). Natural convection during solidification of an alloy from above with application to the evolution of sea ice. *Journal of Fluid Mechanics*, 344, 291–316.
- Worster, M. G. (1992). Instabilities of the liquid and mushy regions during solidification of alloys. *Journal of Fluid Mechanics*, 237, 649–669.
- Xia, W., and M. F. Thorpe (1988). Percolation properties of random ellipses. *Physical Review A*, 38(5), 2650–2656.
- Yi, Y.-B., and A. M. Sastry (2004). Analytical approximation of the percolation threshold for overlapping ellipsoids of revolution. *Proceedings of the Royal Society of London, Series A*, 460, 2353–2380.
- Zhang, S., M. S. Paterson, and S. F. Cox (1994). Porosity and permeability evolution during hot isostatic pressing of calcite aggregates. *Journal of Geophysical Research*, 99(B8), 15,741–15,760.

Table captions

Table 1: Average properties and heat balance for sea ice growth simulations in a domain $0.72 \text{ m} \times 1.44 \text{ m}$, with a constant surface temperature of -20°C at the time the freezing front of the sea ice sheet has reached 1.08 m . The grid size is 12×24 .

Table 2: Parameters α and β determined from the percolation model in domains 2000×2000 (2D, squares), $200 \times 200 \times 200$ (3D, cubes), and in the sandwich domain ($a_0 = 1000$, $d_0 = 195.1$, $\Delta y = \Delta z = 200$).

Tables

Table 1

$1 - f_i$	0.1	0.2	0.5	0.8
$t_{1.08\text{m}} (10^6 \text{ s})$	5.0	5.4	6.3	10
$\overline{F}_c (\text{W m}^{-2})$	-65	-63	-60	-54
$\overline{F}_a (\text{W m}^{-2})$	4	6	9	23
$\overline{F}_h (\text{W m}^{-2})$	-61	-57	-51	-31

Table 2

	2D	3D	sandwich
fit interval $f_t - f_c$	$[2, 6] \times 10^{-2}$	$[1, 10] \times 10^{-2}$	$[3, 30] \times 10^{-3}$
α	1.050	0.890	0.337
β	0.149	0.404	0.406
f_c	0.667	0.277	0.0540

Figure captions

Figure 1: One-dimensional example of the solid volume fraction profile close to the interface. Linear extrapolation of the solid volume fraction of two neighbouring cells (performed in both x -direction and y -direction of the domain separately) is used to determine the virtual solid volume fraction $1 - f_i$ at the interface.

Figure 2: Gravity drainage data of Cox and Weeks (1975), Figures 30 and 31. Temperature gradients in K m^{-1} : (\cdot) 10 to 60; (\circ) 60 to 120; (\times) 120 to 180. The linear fit function (10) of Cox and Weeks (1988) with $f_c = 0.050$ (broken line), and the fitted power law (11) with $f_c = 0.054$ and exponent 1.2 (solid line) are shown.

Figure 3: Perpendicular components of sea ice permeability Π_{h1} and Π_{h2} horizontally, and Π_v vertically.

Figure 4: Schematic of the simplified typical desalination flow path used to estimate the relationship between isotropic permeability Π and vertical permeability component Π_v .

Figure 5: Comparison of salinity profiles predicted from (18) (dotted lines) and computed (data points and solid lines) with permeability function (28) for surface temperatures -10°C (crosses) and -20°C (dots). Shown are (a) scatter plots of eight calculations (bottom data not shown), and (b) two complete profiles. Note the different scales.

Figure 6: Salinity profiles of ice sheets of different $1 - f_i$ at the time the freezing front of the sea ice sheet has reached 1.08 m. Ice growth is from a surface at a constant temperature of -20°C in a domain $0.72\text{ m} \times 1.44\text{ m}$. The grid size is 12×24 , and the domain is periodic horizontally. Simulated salinity data (markers) are compared with the expected salinity profiles (lines) which are based on the simulated growth velocity, w , and equation (18).

Figure 7: Schematic of the periodic stacking of brine layers and ice platelets in sea ice (sandwich model). The brine layer width is d_0 , and the platelet spacing is $a_0 = \Delta x$.

Figure 8: Effective porosity f_e as a function of (a) total porosity f_t , and (b) total porosity above critical porosity $f_t - f_c$ for the cases of two-dimensional (2D), three-dimensional (3D), and sandwich model domains. The dotted lines follow $f_e = f_t$. The critical porosity f_c appropriate for each domain is used in (b). The thin lines in (b) are the best fit power law functions (33) with parameters listed in Table 2. Note the different scales in (a) and (b).

Figure 9: Vertical permeability as a function of total porosity. This work (solid), Eicken et al. (2004) (dashed), scaled Freitag (1999) young ice (dash-dot), scaled Freitag (1999) old ice (dotted). Data points are the data of Saeki et al. (1986) (squares); the data of Ono and Kasai (1985) and Saito and Ono (1978), scaled by Maksym and Jeffries (2000) (crosses); and the scaled data of Cox and Weeks (1975) (gray dots).

Figures

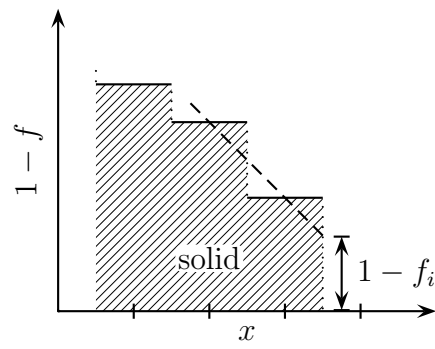


Figure 1

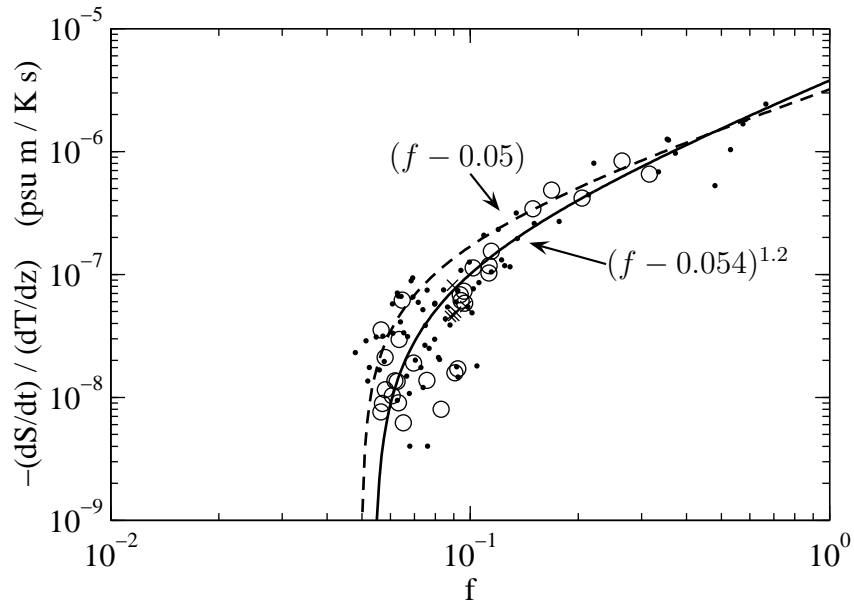


Figure 2

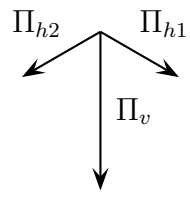


Figure 3

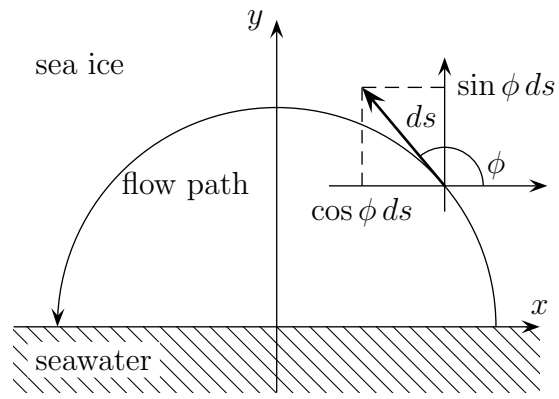


Figure 4

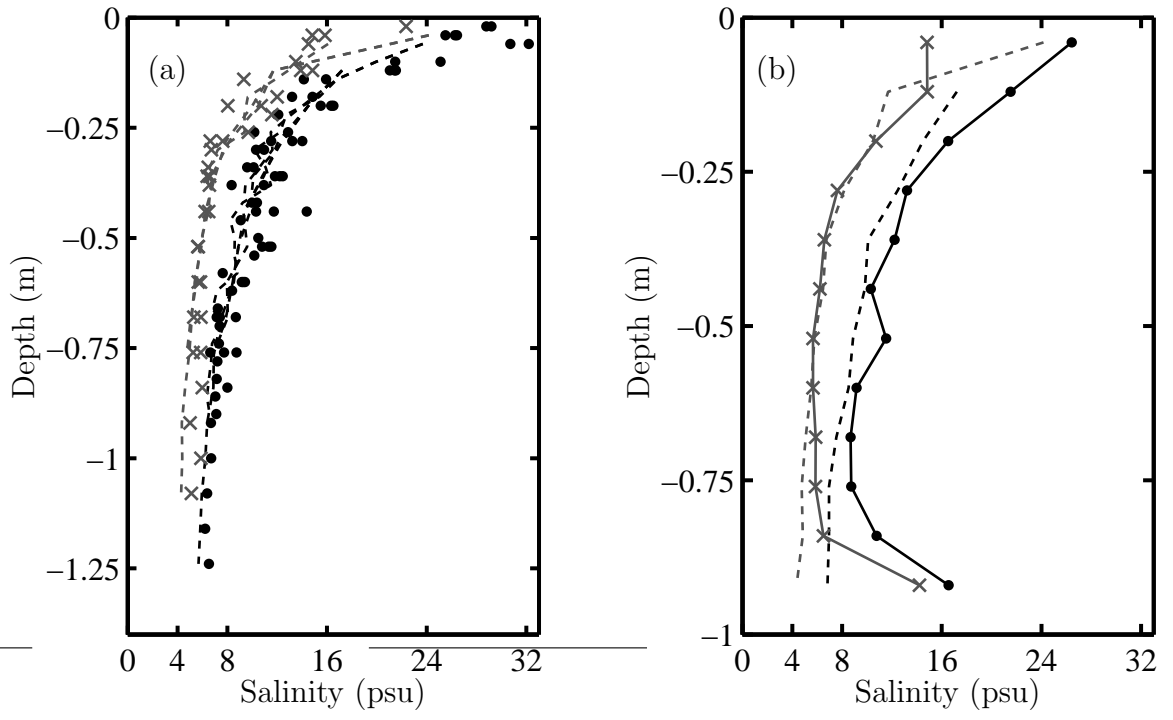


Figure 5

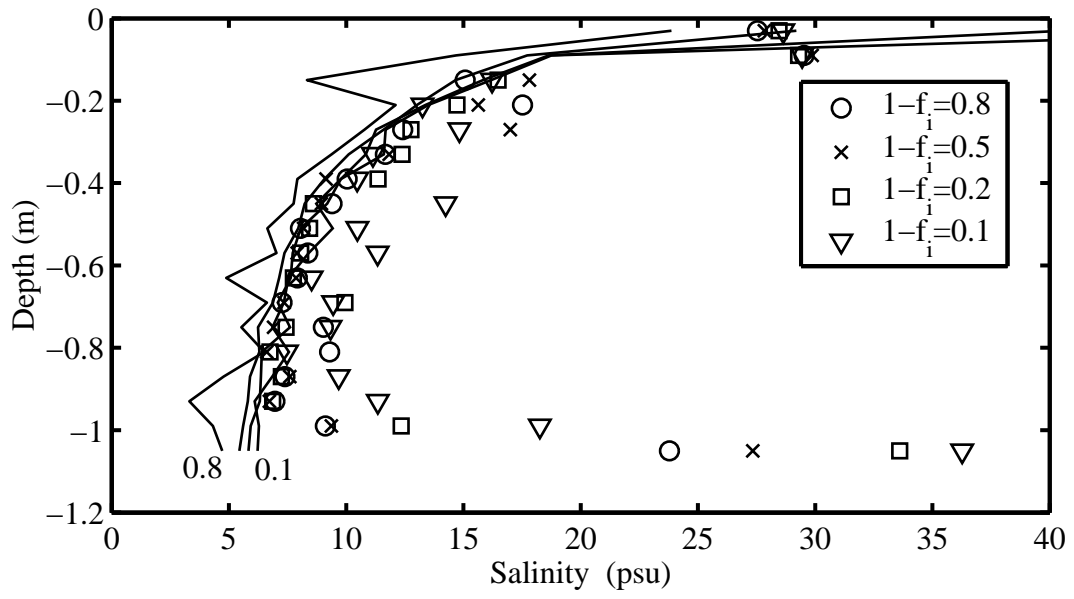


Figure 6

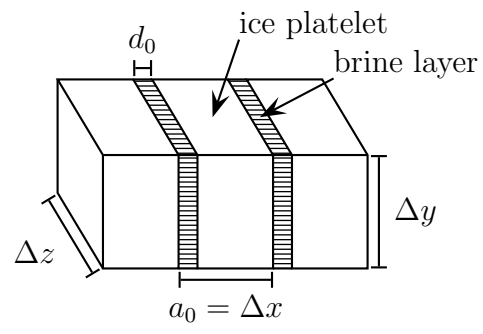


Figure 7

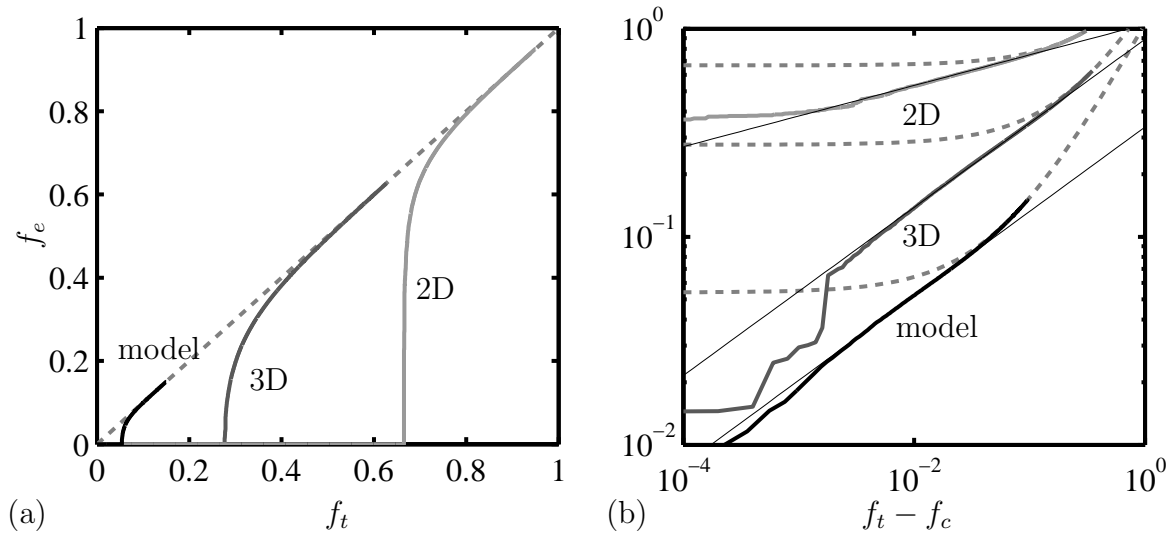


Figure 8

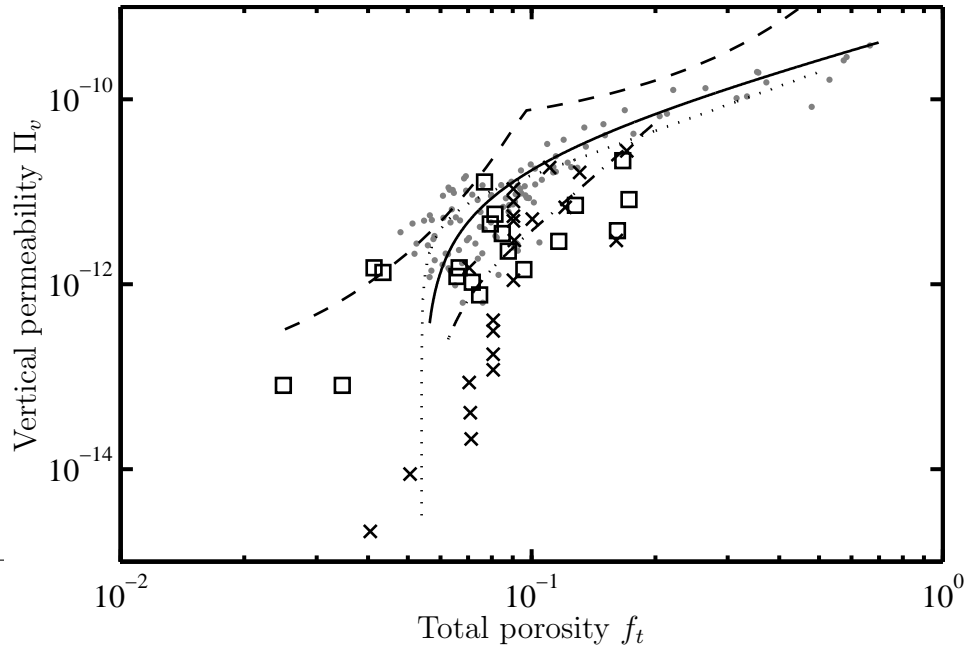


Figure 9